Chapter 5
Scanning-Probe Electronic Imaging of Lithographically Patterned Quantum Rings

F. Martins, D. Cabosart, H. Sellier, M.G. Pala, B. Hackens, V. Bayot and S. Huant

Abstract Quantum rings patterned from two-dimensional semiconductor heterostructures exhibit a wealth of quantum transport phenomena at low temperature and in a magnetic field that can be mapped in real space thanks to dedicated scanning probe techniques. Here, we summarize our studies of GaInAs- and graphene-based quantum rings by means of scanning-gate microscopy both at low magnetic field, where Aharonov-Bohm interferences and the electronic local density-of-states are imaged, and at high magnetic field and very low temperatures, where the scanning probe can image Coulomb islands in the quantum Hall regime. This allows decrypting the apparent complexity of the magneto-resistance of a mesoscopic system in this regime. Beyond imaging and beyond a strict annular shape of the nanostructure, we show that this scanning-probe technique can also be used to unravel a new counter-intuitive behavior of branched-out rectangular quantum rings, which turns out to be a mesoscopic analog of the Braess paradox, previously known for road or other classical networks only.

F. Martins (✉) · D. Cabosart · B. Hackens · V. Bayot
Université Catholique de Louvain, IMCN/NAPS, Louvain-La-Neuve, Belgium
e-mail: fredmarte@hotmail.com

B. Hackens
e-mail: benoit.hackens@uclouvain.be

V. Bayot
e-mail: vincent.bayot@uclouvain.be

H. Sellier · S. Huant
Université Grenoble Alpes, CNRS, Institut Néel, 38000 Grenoble, France
e-mail: hermann.sellier@neel.cnrs.fr

S. Huant
e-mail: serge.huant@neel.cnrs.fr

M.G. Pala
C2N, CNRS, Univ Paris-Sud, Université Paris-Saclay, 91405 Orsay, France
e-mail: marco.pala@c2n.upsaclay.fr

© Springer International Publishing AG, part of Springer Nature 2018

V.M. Fomin (ed.), *Physics of Quantum Rings*, NanoScience and Technology,
https://doi.org/10.1007/978-3-319-95159-1_5

5.1 Introduction

Electron systems confined in mesoscopic quantum rings (QRs) patterned from two-dimensional charge carrier systems exhibit a wealth of quantum transport phenomena at low temperature and in a magnetic field such as the Aharonov-Bohm effect (AB) or the quantum Hall effect (QH). These effects have usually been observed thanks to measurements of the device electrical resistance vs the magnetic field. Such data yield "global" information on the phenomenon, i.e. on the scale of the device. During the last fifteen years, numerous attempts have been made to obtain real-space information on these mesoscopic phenomena down to the nanometer scale (i.e. on a smaller scale than the device size), thanks to dedicated scanning probe techniques. Mapping locally these phenomena give new insights, which allow for a more in-depth comparison with simulations. This chapter focuses on GaInAs- and graphene-based open QRs that are imaged by scanning-gate microscopy (SGM), a variant of electric atomic-force microscopy (AFM), which can access to the intimate behavior of buried electronic systems, not accessible to the tip of scanning tunneling microscopy (STM).

After a brief introduction to SGM in Sects. 5.2 and 5.3 focuses on the low-magnetic field range where the conductance modulations of a ring device induced by the scanning probe provide rich patterns that are either concentric or radial with the ring geometry. The concentric patterns, primarily seen when the tip scans outside the ring area [1], image in real space the AB interferences taking birth in the ring device as a consequence of its ability to capture a magnetic flux or to differentially probe in its two arms a remote electrostatic potential. Radial patterns, that are seen when the probe scans directly over the ring, indirectly map the electronic local density of states (LDOS) at the Fermi energy [2, 3], as does STM in a direct way for surface electron systems [4]. Quantum simulations give a limit to the range of validity for the correspondence between conductance and LDOS maps and show how robust this correspondence can be against, for example, the introduction of impurities in the ring materials [5].

Beside conventional semiconductor systems, the last decade has witnessed the advent of new types of materials with unusual charge carrier dynamics. The most striking example is graphene, a two-dimensional crystal of carbon atoms arranged on a honeycomb lattice [6]. Charge carriers in graphene behave as massless relativistic particles and novel properties emerge in particular close to the Dirac point, where valence and conduction bands touch. Section 5.4 focuses on QRs carved out of graphene, and examine the consequences of the peculiar band structure and charge carrier dynamics on scanning gate imaging of coherent transport in such devices. In particular, radial patterns were also imaged in disordered graphene rings [7], and they were found to be recurrent when varying the charge carrier energy [8]. The observation is consistent with an earlier theoretical prediction of "relativistic quantum scars" [9] , i.e. semiclassical orbits scarring the LDOS.

At high magnetic field, which is the focus of Sect. 5.5, the charge carrier system enters into the QH regime, where electrons should only be transmitted through spatially separated edge states (ESs) near integer filling of the Landau levels. In contrast

to extended 2D systems that exhibit vanishing longitudinal resistance concomitant to Hall plateaus in the QH regime, mesoscopic devices lead to surprising observations [10], such as pseudo-AB oscillations with "sub-periods" and "super-periods" compared to the orthodox AB oscillations seen at low field. To explain these observations, recent models [11] put forward the theory that, when counter-propagating ES come close to each other, electrons can hop between ES, or tunnel through quantum Hall insulating islands. Such islands, also called localized states, are made of ES rotating around hills or dips in the potential landscape, or around the central antidot in a ring geometry. SGM reveals to be very powerful in locating QH islands in GaInAs QRs, and in revealing the spatial structure of transport inside the QH interferometer that they form [12]. Locations of QH islands are found by modulating, with the scanning tip, the tunneling between ESs and confined electron orbits. Tuning the magnetic field, SGM unveils a continuous evolution of active QH islands [12]. This allows decrypting the complexity of high-magnetic field magnetoresistance oscillations, and opens the way to further local-scale manipulations of QH localized states.

In Sect. 5.6 we consider the possibility to control the electron transport through the buried semiconductor nanostructure by means of the SGM tip. In doing so, we find evidence for a counterintuitive behavior of mesoscopic networks [13] that presents a striking similarity with the Braess paradox encountered in traffic or classical networks [14]. A simulation of quantum transport in a two-branch mesoscopic network of rectangular shape reveals that adding a third branch can paradoxically reduce transport efficiency. This manifests itself in a sizable conductance drop of the network. A SGM experiment using the tip to modulate the transmission of one branch in the network reveals the occurrence of this paradox by mapping the conductance variation as a function of the tip voltage and position [13].

5.2 A Brief Introduction to the Technique of Scanning-Gate Microscopy

Unlike common AFM-based imaging techniques, scanning gate microscopy does not rely on a measurement of the cantilever property (i.e. its deflection angle, or resonance frequency shift), but rather of the device electrical characteristics. The principle of SGM [15–17] is sketched in Fig. 5.1. A voltage-biased (V_{tip}) metal-coated AFM tip is laterally scanned at an altitude of a few tens of nm over the device surface to perturb locally its electrical conductance G (or resistance). The changes in the device conductance ΔG are mapped as a function of the relative tip-sample position (x,y) to draw a $\Delta G(x,y)$ SGM map. Depending on the device impedance, a current-biased device (I) or voltage-biased (V) configuration can be used. The whole setup is immersed into a cryostat to operate down to below 100 mK for the coldest SGM setups [12, 18]. Optionally, an external magnetic field can be applied. The combined low-temperature and magnetic field environment requires the use of cryogenic magnetic-free displacement units, such as for example titanium-made

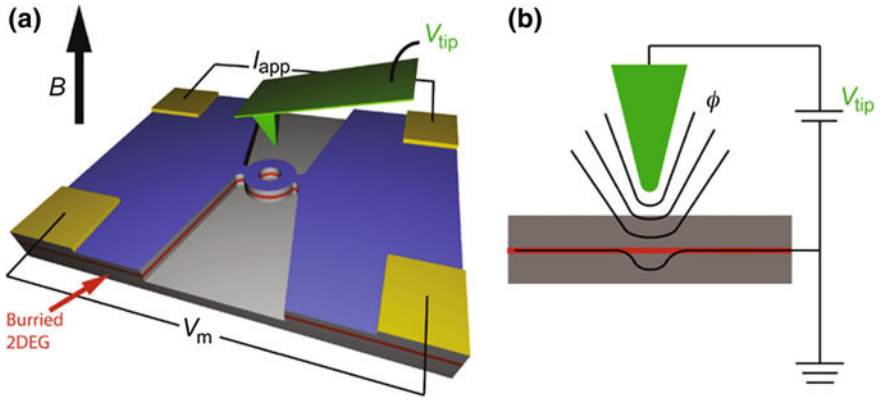

Fig. 5.1 Principle of scanning-gate microscopy. Frame **a** depicts a sketch of a SGM experiment on a ring-shaped device that hosts a buried 2DEG. A current I_{app} is applied to the device and the voltage drop V_m across it is measured, while the biased tip (V_{tip}) is raster scanned over the device. A perpendicular magnetic field $\boldsymbol{B}$ is applied. In frame **b**, curved lines sketch the tip-induced isopotential lines ϕ felt by the buried electron system. For a sufficiently negative tip voltage, a depleted region is formed below the tip in the case of semiconductor 2DEGs (not for graphene)

inertial step motors [19, 20] for the in situ coarse positioning of the tip relative to the nanostructure over a few millimeters. In our setup, fine positioning over a few micrometers for image acquisition is ensured by commercially available piezoelectric scanner elements.

Using an AFM environment allows for locating the active device by measuring the sample topography, e.g. by using the dynamic mode of the AFM. Instead of using an optical method to measure the AFM cantilever deflection, as commonly done in AFM, it is advantageous to use a light-free setup [21], so that photosensitive devices remain under dark conditions during the entire experiment. One solution consists in gluing the AFM cantilever on a piezoelectric tuning fork, and monitoring the shift Δf of its resonance frequency observed when the tip approaches the surface. Sample topography is performed by using a feedback loop on Δf while scanning the tip over the device surface. Once the device topography has been mapped, SGM is performed by lifting the tip at some tens of nanometers (typically 20–50 nm) above the surface and scanning it along a plane parallel to the 2D electron gas (2DEG), with a voltage applied to the tip. SGM measurements are carried out without contact between tip and sample, so that there is no electrical current through the tip, which acts indeed as a flying nanogate.

SGM has been used to image a broad range of transport-related phenomena in various nanostructures, such as for example the branching of conductance channels transmitted through quantum-point contacts (QPCs) [16, 17, 22], magnetic steering in a series of connected QPCs [23], Coulomb blockade in quantum dots [24–26], scarred wavefunctions in quantum billiards [27], and various graphene-based nanodevices [28–35], including in the quantum Hall regime [34]. We refer the reader to [36] for a

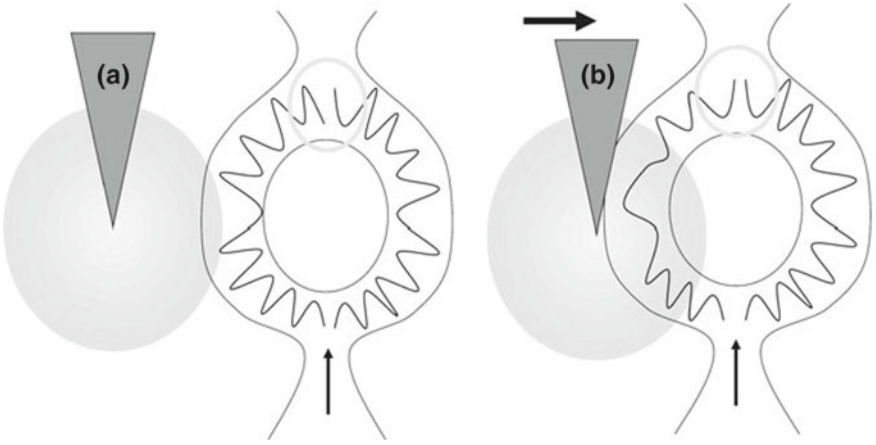

Fig. 5.2 Sketch of the electrostatic AB effect in a QR due to the tip bias. The cone and disk stand for the tip and potential range, respectively. Approaching the tip to the QR from the left modifies the electrostatic potential felt by the electrons in the left arm, tuning the wavefunction interference at the output of the device from destructive (**a**) to constructive (**b**)

more extensive review. In the rest of this chapter, we focus on our own work devoted to GaInAs- and graphene-based QRs.

5.3 Imaging of Quantum Rings in the Low-Field Aharonov-Bohm Regime

If electrons maintain their phase coherence over sufficiently long distances, an open QR sees its conductance peaking when electron waves interfere constructively at the output contact, and decreasing to a minimum for destructive interference. Varying either the electrostatic potential in one arm, e.g., by approaching the SGM biased tip as shown schematically in Fig. 5.2, or the magnetic flux captured by the QR allows the interference to be tuned. This gives rise to the electrostatic [37] and magnetic [38] AB oscillations in the ring conductance.

These interference phenomena can be imaged in real space by SGM [1]. An example of such imaging is shown in Fig. 5.3. Here, the QR is patterned from a $Ga_{0.3}In_{0.7}As$-based heterojunction with carrier concentration and mobility at 4.2 K of 2.0×10^{16} cm^{-2} and 100.000 cm^2 V^{-1} s^{-1}, respectively. The QR is connected to the 2D electron reservoir, which is buried 25 nm below the free surface, by two upper and lower narrow constrictions. The mean-free path and coherence length in $Ga_{0.3}In_{0.7}As$ at 4.2 K are 2 and 1 μm, respectively, so that the electron transport is in the ballistic and (partly) coherent regimes. The coherent nature is confirmed

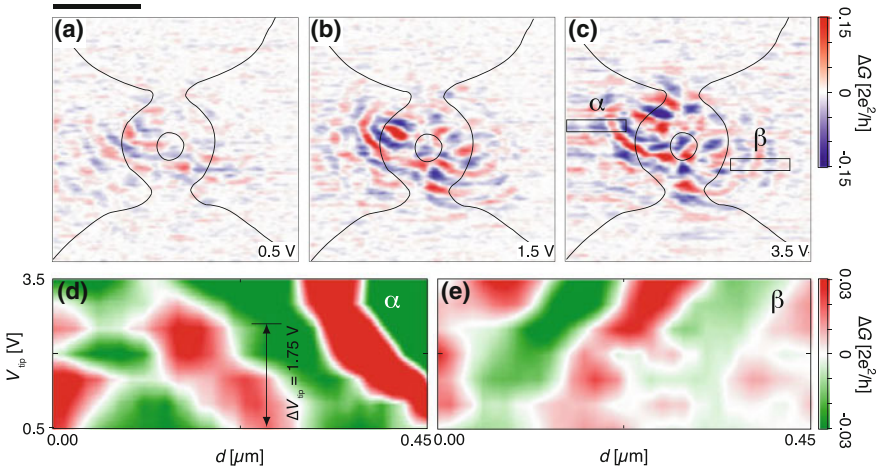

Fig. 5.3 SGM images (**a**–**c**) of a GaInAs QR whose geometry is shown schematically by full lines (image size: 2 μm × 2 μm; T = 4.2 K; zero magnetic field). The inner and outer ring diameters are 210 and 610 nm, respectively. The images are acquired for different tip voltages V_{tip} indicated on the figures and are all filtered [1] to compensate for a slowly varying strong background, which masks part of the interference pattern. Frames d and e are two sequences of profile plots as function of the tip bias. Each horizontal line corresponds to a vertical average of the conductance map in regions (α) and (β) shown in Fig. 5.3c, respectively. Adapted from [39]

by the observation of AB oscillations in the magneto-conductance when the QR is subjected to a perpendicular magnetic field [1].

One also observes an electrostatic AB effect which gives rise, at low magnetic field, to a well-developed fringe pattern in the SGM conductance image of the QR when the tip scans outside the QR. This outer pattern is mainly concentric with the ring geometry, as can be seen in the sequence of images shown in Fig. 5.3a–c obtained at different voltages applied to the tip. The interference pattern is here best seen on the left part of the ring, possibly due to a ring asymmetry. The qualitative interpretation in terms of a scanning-gate-induced electrostatic AB effect is that as the tip approaches the QR, either from the left or right, the electrical potential mainly increases on the corresponding side of the QR (see Fig. 5.2). This induces a phase difference between electron wavefunctions traveling through the two arms of the ring, and/or bends the electron trajectories, tuning the interference alternatively from constructive to destructive, thereby producing the observed pattern. Figure 5.3d, e shows how the interference pattern evolves for increasing tip voltages when the tip scans over the left hand-side and right hand-side regions of the QR, respectively [39]. It is clear from this figure that for increasing tip voltages the interference fringes shift away from the QR to the left in d and to the right in e, respectively. This is a direct manifestation of the tip-induced electrostatic AB effect. From Fig. 5.3d, we find that a phase shift of π is obtained for a tip bias variation $\Delta_{tip} = 1.75$ V [39].

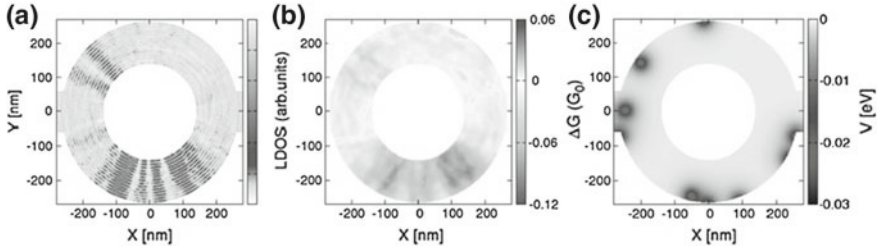

Fig. 5.4 Quantum simulation of a SGM experiment on a QR in the presence of positively charged impurities. The outer diameter, inner diameter and opening width are 530, 280, and 120 nm, respectively. The effective mass is 0.04 m_0 as in GaInAs (m_0 is the free electron mass). The Fermi energy is $E_F = 107.4$ meV. Frames **a** and **b** are simulated images of the LDOS and conductance changes (in units of G_0, the quantum of resistance), respectively, calculated for the random distribution of positively-charged impurities shown in frame (**c**). In the simulation, the tip potential has a Lorentzian shape with 10 nm range and amplitude $E_F/50$. Adapted from [5]

Now, modifying the magnetic field strength, another phase term contributes through the magnetic AB effect, i.e. the capture of the magnetic flux threading the QR area. The flux periodicity of such oscillations correspond to the flux quantum $\phi_0 = h/e$. This displaces the whole fringe pattern with respect to the QR. This displacement is periodic in magnetic field strength with the same periodicity (here 13 mT, in nice agreement with the average area of the QR) than the AB oscillations seen in the magneto-conductance [1, 39], which gives further support to the interpretation in terms of AB effects. This interpretation was confirmed by density functional theory [40].

In Fig. 5.3a–c, it is clear that the conductance images also exhibit a complex pattern when the tip scans directly over the QR region. These inner fringes are linked to the local electron-probability density in the QR [2, 3, 5], provided that the tip potential is weak enough not to distort the QR electron density (see also [40]). A detailed analysis based on quantum mechanical simulations of the electron probability density, including a model tip potential, the magnetic field, and randomly distributed impurities, reproduces the main experimental features and demonstrates the relationship between SGM conductance maps and electron probability density, i.e. LDOS, at the Fermi energy. An example of such a relationship is shown in Fig. 5.4 in the case of a realistic QR perturbed by positively charged impurities (in the experiments on $Ga_{0.3}In_{0.7}As$ heterojunction devices, the electrostatic potential experienced by electrons is influenced by ionized dopants located a few nm above the conducting 2D electron system). Although impurities distort the LDOS, this distortion is reflected back in the conductance image in such a way that the conductance map can still be seen as a mirror of the electronic LDOS. As shown in Fig. 5.4, both the LDOS and conductance images tend to develop radial fringes, which are mostly, but not entirely, anchored to the impurity locations.

The discussion above suggests that SGM can be viewed as the analog of STM [4] for imaging the electronic LDOS in open mesoscopic systems buried under an

insulating layer. It can also be seen as the counterpart of the near-field scanning optical microscope that can image photonic [41, 42] LDOS in confined nanostructures, provided that the excitation light source can be considered as point-like such as in active tips based on fluorescent nano-objects [43].

5.4 Recurrent Quantum Scars in Graphene Quantum Rings

In a semiclassical framework, the inner radial fringes observed in the arms of QRs (discussed in previous section) can be viewed as "privileged paths" along which charge carrier wavefunctions are concentrating, also named "scarred wavefunctions", or "scars". Such scars have been introduced in the framework of quantum chaos theories [44]; in the latter case, they were associated with unstable semiclassical periodic orbits in quantum billiards. A specific aspect of semiclassical periodic orbits, useful for probing their existence in the experiment, is their recurrence originating from their finite orbit length: scar patterns associated with such semiclassical periodic orbits were predicted to reappear periodically with the Fermi energy E_F in relativistic systems like graphene while the recurrence should occur with the square root of E_F in the case of a conventional semiconductor system [9].

This prediction was investigated using SGM, through experiments realized on two different graphene QRs, fabricated from exfoliated graphene, transferred either directly on top of a degenerately doped oxidized silicon substrate acting as a back-gate [7], or on hexagonal boron nitride (h-BN) deposited on top of a similar silicon substrate [8]. In the first case, the measured low temperature mobility of charge carriers was relatively modest (around 1000 cm^2/Vs). In the low density regime (close to the Dirac point), SGM reveals Coulomb blockade oscillations, associated with disorder-induced localized states. Such localized states are ubiquitous in low-mobility graphene devices at low charge carrier density since the disorder landscape induces randomly located electron and hole puddles which can constitute and act like isolated quantum dots, tunnel-coupled with the transmitted channels. They have already been imaged indirectly using tip-induced tuning of Coulomb blockade in various SGM experiments, in particular in small constrictions [31–33]. In contrast, at higher charge carrier densities, disorder is at least partially screened and electron/hole puddles disappear. In these conditions, SGM imaging on the graphene QR revealed radial fringes (scars) [7] very similar to those found in heterostructure-based QRs [2]. Simulations realized on graphene QR with similar degree of disorder confirmed that radial patterns naturally emerge at various locations along QR's arms in the LDOS.

The recurrence of the radial pattern of scars with energy was studied using SGM in another graphene QR with higher charge carrier mobility (~10000 cm^2/Vs), deposited on top of an h-BN flake [8]. A large number of radial scars was observed in this case, and sequences of SGM images obtained at various back-gate voltage were thoroughly examined, in order to find evidence of recurring patterns. Cross-correlations

between successive images were calculated, both for full SGM images and for specific areas on SGM images where radial patterns were observed. Local maxima in the correlation parameters were found when varying the Fermi energy, clearly indicating the energy recurrence, with an average distance between maxima varying slightly depending on the examined portion of the SGM image. This distance in energy can be directly converted in semiclassical orbit lengths corresponding to twice the QR arm width, which allowed to associate the sequence of maxima in SGM image correlation parameters with radial scars. Note that similar energy recurrence was also found for patterns of radial scars obtained in simulated QR LDOS.

5.5 Imaging Quantum Rings in the Quantum Hall Regime

In the two previous sections we focused on transport at zero or low-magnetic field (B) through a QR. The wave-like nature of electrons could be revealed by periodic AB oscillations in the magneto-resistance of the device. They originate from the different phases that electrons acquire along both arms of a QR when B is applied perpendicular to the 2D electron system. In this section, we will discuss another type of periodic magneto-resistance oscillations, which show up at high B in QRs.

At high magnetic field the electron transport picture changes drastically as the cyclotron radius shrinks, highly degenerate Landau levels (LLs) form and the 2DEG enters in the "QH regime". When the Fermi energy lies between two Landau levels (i.e. around integer LL filling factor ν), the bulk of the 2DEG becomes insulating and current flows through counter-propagating one-dimensional channels, the so-called ESs, confined along the borders of the device, where the Fermi energy crosses LLs. In macroscopic devices, scattering between opposite ESs vanishes and the electron mean free path becomes of the order of several millimeters. Moreover, QH islands (QHIs), i.e. electrons trapped in closed ESs pinned around potential inhomogeneities, remain electrically isolated and do not contribute to electron transport. This gives rise, as shown in Fig. 5.5a, to plateaus in the transverse resistance R_{xy}, and to a vanishing longitudinal resistance R_{xx} measured in a macroscopic Hall bar (for review see e.g. [45]).

However, when the size of the device is reduced and becomes comparable with the size of QHIs, this picture is no longer valid. In such conditions, several experiments have reported "sub-periodic" and "super-periodic" magnetoresistance oscillations, i.e. with a flux period corresponding to a fraction, or a multiple of the usual AB period observed at low-magnetic field (see sections above) [10, 46–51]. Driven by these intriguing results, theoretical efforts have explained these oscillations within a model where Coulomb interactions dominate [11]. In small devices, the counter-propagating ESs are indeed brought close to each other so that electrons may tunnel between them, either directly, and/or through a QHI that mediates electron transmission [52, 53]. Rather than coherent effects, the discrete nature of electrons has naturally been put forward.

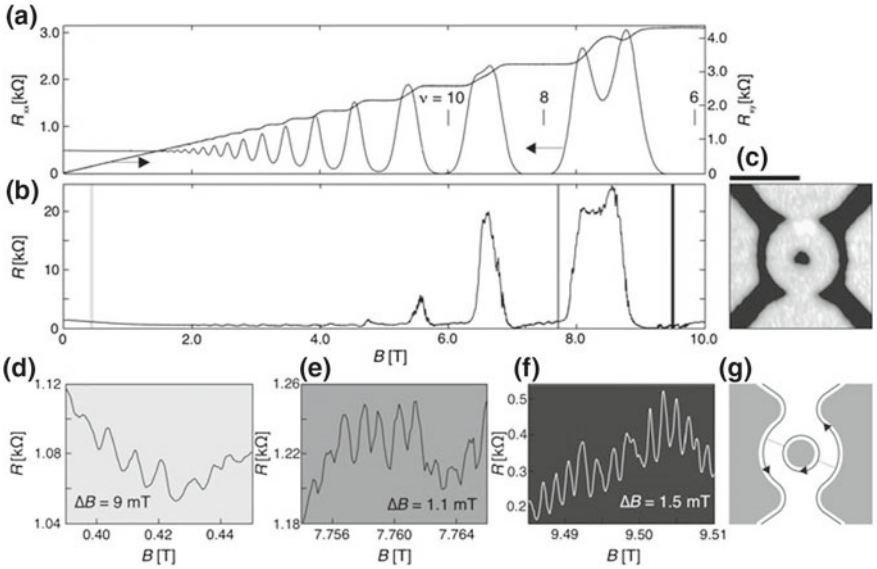

Fig. 5.5 Quantum Hall effect on a mesoscopic QR. In **a** the black and red curves are the longitudinal (*Rxx*) and the transverse (*Rxy*) resistances of a Hall bar, respectively, as function of the magnetic field (*B*). At high *B*, *Rxy* is quantized in $e^2/(N.h)$, where *N* is the number of fully occupied Landau levels, while *Rxx* becomes zero. The AFM micrograph of the QR is shown in **c** where the black bar represents 1 μm. In **b** we display the magnetoresistance measured across the QR in the same range of *B* and at a temperature $T = 100$ mK. Close-ups of **b** are shown in (**d**–**f**). At low-*B* (**d**), the periodicity of the oscillations is $\Delta B_{AB} = 9$ mT which, given the geometry presented in (**c**), is consistent with AB interferences. At high magnetic field, for $N = 8$, shown in (**e**) the periodicity is $\Delta B = 1.1$ mT while, for $N = 6$, displayed in (**f**), we find $\Delta B = 1.5$ mT. The latter oscillations are explained, as sketched in (**g**), as tunneling between edge states through a Coulomb island located around the central anti-dot of the QR. This gives rise to periodic oscillations with $\Delta B.N = \Delta B_{AB}$

The experiments discussed in this section [12] are performed at a temperature $T = 100$ mK, inside a ^{3}He/^{4}He dilution refrigerator, equipped with a superconducting coil that can provide a magnetic field up to 15/17 T. The 2DEG in which the QR is patterned is located 25 nm below the surface and, at low-*T*, the electron density and mobility are 1.4×10^{16} m^{-2} and 4 m^2/Vs, respectively. Figure 5.5c shows the device topography. The QR has an average outer diameter of 1 μm, two apertures and a central antidot diameter of approx. 300 nm. The magneto-resistance of the quantum ring (*R* versus *B*), measured simultaneously with R_{xx} and R_{xy} in the bulk, is shown in Fig. 5.5b, d–f. Figure 5.5b shows *R* versus *B* over the full magnetic field range, from 0 to 10 T. At low magnetic field, Fig. 5.5d, periodic AB oscillations with $\Delta B_{AB} = 9$ mT are observed. This is consistent with an average radius of 380 nm for the QR. In Fig. 5.5e, f, two *B*-ranges are zoomed, around $\nu = 8$ and 6, respectively. In these ranges the magnetoresistance of the device displays oscillations with two different "sub-periods": $\Delta B = 1.1$ mT around $\nu = 8$ and, around $\nu = 6$, $\Delta B = 1.5$ mT. As sketched in Fig. 5.5g, one can understand these oscillations within a Coulomb-

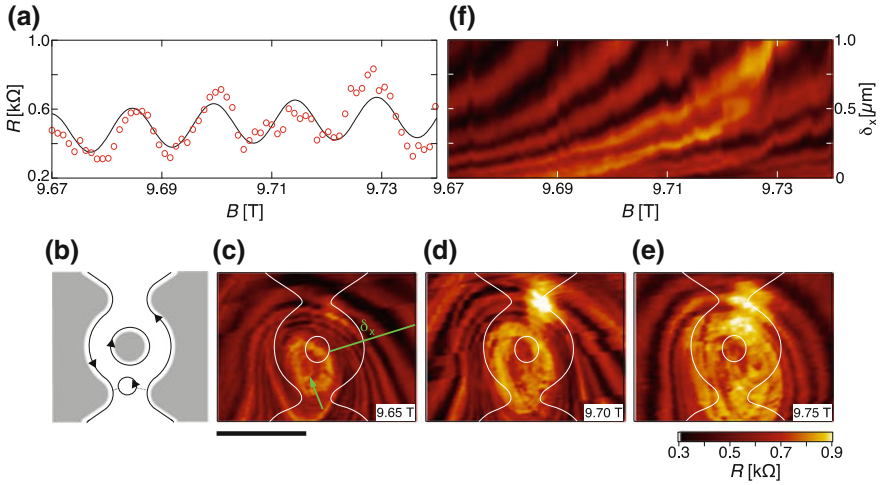

Fig. 5.6 Identification of the centre of a Coulomb island inside a QR using SGM. Frame **a** shows R versus B in the range $B = [9.67\ \text{T}, 9.74\ \text{T}]$. The periodicity of the fringes is $\Delta B = 17$ mT, which corresponds to a QHI with a surface equivalent to a disc of radius ~65 nm located, as sketched in (**b**), somewhere in the arms of the 300-nm-wide QR. **c**–**e** are SGM resistance maps obtained at $B = 9.65$, 9.70 and 9.75 T, respectively, with $V_{tip} = -1$ V. The white lines correspond to the position of the QR and the scale bar represents 1 μm. This sequence of images reveals the position of the center of the QHI [marked with a green arrow in (**c**)], inside the QR. **f** depicts B-dependence of the $R(x, y)$ profile measured along the green line in **c**, $V_{tip} = -1$ V. The fringes share the same periodicity $\Delta B = 17$ mT as in (**a**)

dominated model where electrons tunnel between propagating ESs through a QHI with discrete energy levels, located around the central anti-dot of the QR [11]. The basis of this model is that a change in magnetic field induces a periodic change in the QHI energy with respect to the ES energy. For each flux quantum added to the QHI, one electron has to be added to each populated ES in the QHI, which means that, in this case, Coulomb blockade oscillations are observed, with a period:

$$\Delta B = (\varphi_0/A)/N;$$

where N is the number of filled ESs around the QHI of area A. Indeed, the periods measured in Fig. 5.5e, f are consistent with this relation. Nevertheless, shifting the magnetic field range to $B = [9.67\ \text{T}, 9.74\ \text{T}]$ (still around $\nu = 6$), the magnetoresistance, as displayed in Fig. 5.6a, reveals "super-period" oscillations with $\Delta B = 17$ mT. Using the previous model, we conclude that they correspond to ES loops with a radius of ~65 nm, which would not fit around the QR antidot. However, it could well be located, as drawn in Fig. 5.6b, somewhere in the 300-nm-wide arms of the QR, or near its openings, and be connected to the propagating ES through tunnel junctions.

In order to precisely locate such a QHI, we now use SGM since this technique is particularly well adapted to image electronic transport through buried 2DEG in

the quantum Hall regime [12, 18, 36, 39, 54–59]. Here, we measure the resistance of the device as the electrically polarized AFM tip scans over the surface. Within the Coulomb-dominated model, as the negatively biased tip approaches a QHI, it progressively changes the electrostatic potential experienced by electrons trapped in the QHI and modify the QHI surface which, in turn, induces an energy imbalance between the QHI and the ESs [11, 12]. As with the magnetic field, this imbalance then allows electrons to tunnel between ESs and the QHI in the Coulomb blockade regime, whenever a QHI energy level lies in the energy window defined by the propagating ES potential. In a SGM map, one therefore expects to observe sets of concentric resistance fringes, each one corresponding to a Coulomb blockade peak, encircling each active QHI.

Three consecutive SGM maps for $B = 9.65$, 9.70 and 9.75 T are shown in Fig. 5.6c–e, respectively, where the position of the QR is drawn, superimposed on the SGM data. Concentric fringes are observed, centered close to one of the openings of the QR. As B increases the position of resistance fringes evolves. This is clearly illustrated in Fig. 5.6f, where B is swept while scanning with a negatively polarized tip ($V_{tip} = -1$ V) along the same line, highlighted in green and denoted δx in Fig. 5.6c. As B increases the concentric fringes shift away from their center, indicated by the green arrow in Fig. 5.6c. Importantly, we also note that the periodicity ΔB = 17 mT found in Fig. 5.6f is the same as the one extracted from the magnetoresistance curve in Fig. 5.6a. This allows concluding that the QHI, which is at the origin of these "super-period" oscillations, has its center indicated by the green arrow in Fig. 5.6c.

Remarkably, the slope direction in the plane B versus δx can be used to discriminate between ESs surrounding a potential hill or looping around a potential well. If we assume that a QHI is created around a potential hill, approaching a negatively biased tip will raise the potential and increase the QHI area. On the other hand, in the case of a QHI formed around a potential well, the effect of a negatively biased tip would be to reduce the QHI surface. In Fig. 5.6f, isoresistance lines, that correspond to isoflux states through the QHI, move away from their center as B is raised, which unambiguously indicates that the QHI surrounds a potential hill. Such a potential hill could be caused by the presence of one or several ionized dopants located a few nm above the 2D electron system.

In addition to pinpointing the location of QHIs and understanding their contribution in the high-B magnetoresistance oscillations, SGM can also yield spectroscopic information on QHIs. This is achieved by positioning the tip close to a QHI, and varying the microscope tip bias as well as current bias across the device. This way, we uncovered the QHI discrete energy spectrum arising from electronic confinement and extracted estimates of the gradient of the confining potential, as well as the edge state velocity [58]. Moreover, we also used the SGM tip to modify the configuration of QH edge states in the vicinity of a constriction in order to form a QH interferometer, i.e. a small quantum ring formed by tunnel-coupled QH edge states [59].

5.6 Revealing an Analog of the Braess Paradox in Branched-Out Rectangular Rings

In the above sections, SGM has been used to image the electron transport in annular shaped QRs. In this section, we demonstrate that SGM can also be used to tune the electron transport by depleting, by gate effect, a conduction channel in a branched-out mesoscopic network, whose primary shape is a rectangular ring. This leads to the discovery of a mesoscopic analog [13] of the Braess paradox [14].

Adding a new road to a congested network can paradoxically lead to a deterioration of the overall traffic situation, i.e. longer trip times for road users. Or, in reverse, blocking certain streets in a complex road network can surprisingly reduce average trip time [60]. This counter-intuitive behavior has been known as the Braess paradox [14]. Later extended to other networks in classical physics, such as mechanical or electrical networks [61, 62], this paradox lies in the fact that adding extra capacity to a congested network can counter-intuitively degrade its overall performance. Initially known for classical networks only, we have extended the concept of the Braess paradox to the quantum world [13]. By combining quantum simulations of a model network and SGM, we have discovered that an analog of the Braess paradox can occur in mesoscopic semiconductor networks, where electron transport is ballistic and coherent.

We consider a simple two-path network in the form of a rectangular ring connected to source and drain via two openings (see Fig. 5.7a for the network geometry). In practice, this ring is patterned from a GaInAs heterojunction as for the QRs discussed in the previous sections. The dimensions are chosen to ensure that the embedded 2DEG is in the ballistic and coherent regimes of transport at 4.2 K. The short wires in the ring are chosen to be narrower than the source/drain openings to behave as congested constrictions for propagating electrons. Branching out this ring by patterning a central wire (see Fig. 5.7a) opens a third path to the electrons that bypasses the antidot in the initial rectangular ring. Then, we use SGM to partially block by gate effects the transport through the additional branch. Doing so should intuitively result in a decreased current transmitted through the device, but this is just the opposite behavior that is found in certain conditions, both experimentally and in quantum simulations [13]. Therefore, in a naive picture, electrons in such networks turn out to behave like drivers in congested cities: blocking one path favors "traffic" efficiency.

The above finding is summarized in the simulations of Fig. 5.7a, d, which show the network geometry and a calculated conductance crosscut as a function of tip position, respectively. Here, the outer width and length of the initial corral are 0.75 and 1.6 μm, respectively, whereas the widths of the lateral, upper/lower, and central (additional) arms are $W = 140$ nm, $L = 180$ nm, and $W3 = 160$ nm, respectively. The width of the source and drain openings are $W0 = 320$ nm. This ensures that electron flow in the lateral arms (in the absence of the central arm) is congested because $2\,W < W0$. In other words, all injected conduction channels (about 10) into the network cannot be admitted in these arms [13].

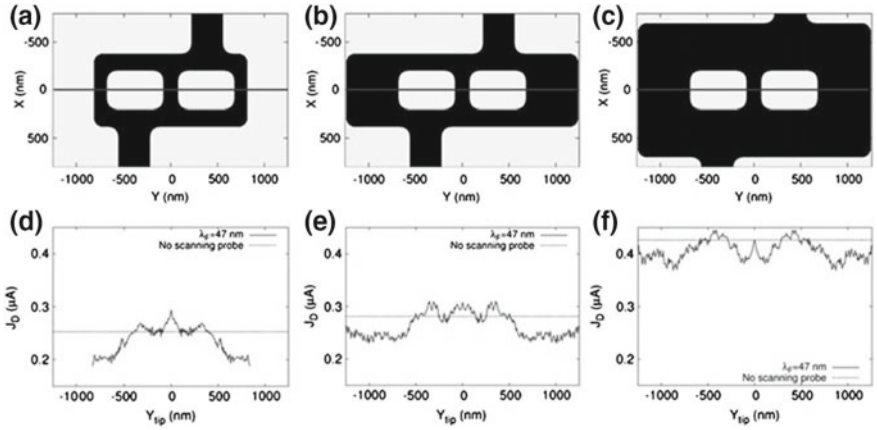

Fig. 5.7 Evidence for a Braess-like paradox in a mesoscopic rectangular network. Frames **a–c** depict the network geometries with parameters given in the text. Frames **d–f** are the corresponding calculated conductance crosscuts in the presence of a depleting SGM tip scanning along the median lines of (**a–c**), respectively. The horizontal dotted lines give the unperturbed conductance without tip. The Fermi wavelength is 47 nm. Fluctuations in the conductance profiles are UCFs due to the tip-induced change in the potential felt by electrons propagating through the device

The crosscut in Fig. 5.7d is obtained by computing the network conductance (source-drain voltage = 1 mV) as function of the tip position scanned along the median line of Fig. 5.7a. This line crosses the lateral and central arms. The tip potential is mimicked by a point-like potential of −1 V placed at 100 nm above the 2DEG [13], which corresponds to a lateral extension of ≈400 nm for the tip-induced potential perturbation at the 2DEG level. This model potential entirely depletes the 2DEG in one arm when the tip passes above it.

It is clear from Fig. 5.7d that depleting the central arm produces a distinctive conductance peak that goes well beyond the unperturbed value. This peak has a much larger amplitude as the universal conductance fluctuations (UCFs) that are seen as small oscillations for any tip position along the median lines, as a consequence of the tip-induced change in the potential felt by electrons propagating through the device [63]. This strong central peak is the signature of the counter-intuitive Braess-like behavior mentioned above. Noteworthy, closing one of the lateral arms reduces the conductance, in agreement with the intuitive expectation: the paradox is seen only when the central branch is closed, not the lateral ones, which stresses the particular role played by this central branch.

Congestion plays a key role in the occurrence of the classical Braess paradox [14, 60, 61]. In order to probe a similar role in the mesoscopic counterpart paradox, we have simulated two additional networks with enlarged lateral arms (Fig. 5.7b, e: W = 560 nm, L unchanged) and with both enlarged lateral and upper-lower arms (Fig. 5.7c, f: W = 560 nm, L = 500 nm) [63]. This releases congestion in the lateral arms. It is clear from Fig. 5.7e, f that releasing congestion smoothens the counter-

intuitive conductance peak seen in the congested network when the central arm is blocked. Nevertheless, there is still a slight conductance (current) increase when the tip scans just above the central arms in networks e and f, but it no longer goes beyond the unperturbed conductance for the largest network f. This finding entails the particular roles played by the additional branch and by network congestion in the occurrence of a distinctive Braess-like paradox. Yet, more experimental and theoretical work is needed to put forward a conclusive explanation at the microscopic level for the paradoxical behavior reported here.

5.7 Conclusion

The few examples presented in this chapter show how powerful is SGM in imaging, and possibly tuning, the electronic transport in ring-shaped semiconductor and graphene devices and to reveal how electrons behave down there. It gives valuable complementary view on phenomena that are usually considered within a macroscopic experimental scheme. The imaging of AB interferences and quantum scars, the ability of locating precisely compressible Coulomb islands in a quantum Hall interferometer, and the closing of a selected branch in a mesoscopic rectangular ring to induce a Braess-like phenomenon, all are illustrative of this claim.

Acknowledgements B. H. and F. M. are associate and postdoctoral researchers respectively with the Belgian FRS-FNRS. This work has been supported by FRFC grant no. 2.4.546.08.F and FNRS grant no 1.5.044.07.F and J.0067.13, by the Belgian Science Policy (Interuniversity Attraction Pole Program IAP-6/42) as well as by the PNANO 2007 program of the Agence Nationale de la Recherche, France ("MICATEC" project). VB acknowledges the award of a "Chaire d'excellence" by the Nanoscience Foundation in Grenoble.

References

1. B. Hackens, F. Martins, T. Ouisse, H. Sellier, S. Bollaert, X. Wallart, A. Cappy, J. Chevrier, V. Bayot, S. Huant, Nat. Phys. **2**, 826 (2006)
2. F. Martins, B. Hackens, M.G. Pala, T. Ouisse, H. Sellier, X. Wallart, S. Bollaert, A. Cappy, J. Chevrier, V. Bayot, S. Huant, Phys. Rev. Lett. **99**, 136807 (2007)
3. M.G. Pala, B. Hackens, F. Martins, H. Sellier, V. Bayot, S. Huant, T. Ouisse, Phys. Rev. B **77**, 125310 (2008)
4. M.F. Crommie, C.P. Lutz, D.M. Eigler, Science **262**, 218 (1993)
5. M.G. Pala, S. Baltazar, F. Martins, B. Hackens, H. Sellier, T. Ouisse, V. Bayot, S. Huant, Nanotechnology **20**, 264021 (2009)
6. K.S. Novoselov, A.K. Geim, S.V. Morozov, D. Jiang, Y. Zhang, S.V. Dubonos, I.V. Grigorieva, A.A. Firsov, Science **306**, 666 (2004)
7. D. Cabosart, S. Faniel, F. Martins, B. Brun, A. Felten, V. Bayot, B. Hackens, Phys. Rev. B **90**, 205433 (2014)
8. D. Cabosart, A. Felten, N. Reckinger, A. Iordanescu, S. Toussaint, S. Faniel, B. Hackens, Nano Lett. **17**, 1344 (2017)
9. L. Huang, Y.C. Lai, D.K. Ferry, S.M. Goodnick, R. Akis, Phys. Rev. Lett. **103**, 054101 (2009)

10. B.J. van Wees, L.P. Kouwenhoven, C.J.P.M. Harmans, J.G. Williamson, C.E. Timmering, M.E.I. Broekaart, C.T. Foxon, J.J. Harris, Phys. Rev. Lett. **62**, 2523 (1989)
11. B. Rosenow, B.I. Halperin, Phys. Rev. Lett. **98**, 106801 (2007)
12. B. Hackens, F. Martins, S. Faniel, C.A. Dutu, H. Sellier, S. Huant, M. Pala, L. Desplanque, X. Wallart, V. Bayot, Nat. Commun. **1**, 39 (2010)
13. M.G. Pala, S. Baltazar, P. Liu, H. Sellier, B. Hackens, F. Martins, V. Bayot, X. Wallart, L. Desplanque, S. Huant, Phys. Rev. Lett. **108**, 076802 (2012)
14. D. Braess, A. Nagurney, T. Wakolbinger, Transp. Sci. **39**, 446 (2005)
15. M.A. Eriksson, R.G. Beck, M. Topinka, J.A. Katine, R.M. Westervelt, K.L. Campman, A.C. Gossard, Appl. Phys. Lett. **69**, 671 (1996)
16. M.A. Topinka, B.J. LeRoy, S.E.J. Shaw, E.J. Heller, R.M. Westervelt, K.D. Maranowski, A.C. Gossard, Science **289**, 2323 (2000)
17. M.A. Topinka, B.J. LeRoy, R.M. Westervelt, S.E.J. Shaw, R. Fleischmann, E.J. Heller, K.D. Maranowski, A.C. Gossard, Nature **410**, 183 (2001)
18. N. Paradiso, S. Heun, S. Roddaro, G. Biasiol, L. Sorba, V. Venturelli, F. Taddei, F. Giovannetti, F. Beltram, Phys. Rev. B **86**, 085326 (2012)
19. C. Obermüller, A. Deisenrieder, G. Abstreiter, K. Karrai, S. Grosse, S. Manus, J. Feldmann, H. Lipsanen, M. Sopanen, J. Ahopelto, Appl. Phys. Lett. **75**, 358 (1999)
20. M. Brun, S. Huant, J.C. Woehl, J.F. Motte, L. Marsal, H. Mariette, J. Microsc. **202**, 202 (2001)
21. K. Karrai, R.D. Grober, Appl. Phys. Lett. **66**, 1842 (1995)
22. B. Brun, F. Martins, S. Faniel, B. Hackens, G. Bachelier, A. Cavanna, C. Ulysse, A. Ouerghi, U. Gennser, D. Mailly, S. Huant, V. Bayot, M. Sanquer, H. Sellier, Nat. Commun. **5**, 4290 (2014)
23. K.E. Aidala, R.E. Parrott, T. Kramer, E.J. Heller, R.M. Westervelt, M.P. Hanson, A.C. Gossard, Nat. Phys. **3**, 464 (2007)
24. A. Pioda, S. Kicin, T. Ihn, M. Sigrist, A. Fuhrer, K. Ensslin, A. Weichselbaum, S.E. Ulloa, M. Reinwald, W. Wegscheider, Phys. Rev. Lett. **93**, 216801 (2004)
25. P. Fallahi, A.C. Bleszynski, R.M. Westervelt, J. Huang, J.D. Walls, E.J. Heller, M. Hanson, A.C. Gossard, Nano Lett. **5**, 223 (2005)
26. A.C. Bleszynski, F.A. Zwanenburg, R.M. Westervelt, A.L. Roest, E.P.A.M. Bakkers, L.P. Kouwenhoven, Nano Lett. **7**, 2559 (2007)
27. R. Crook, C.G. Smith, A.C. Graham, I. Farrer, H.E. Beere, D.A. Ritchie, Phys. Rev. Lett. **91**, 246803 (2003)
28. M.R. Connolly, K.L. Chiou, C.G. Smith, D. Anderson, G.A.C. Jones, A. Lombardo, A. Fasoli, A.C. Ferrari, Appl. Phys. Lett. **96**, 113501 (2010)
29. J. Berezovsky, M.F. Borunda, E.J. Heller, R.M. Westervelt, Nanotechnology **21**, 274013 (2010)
30. J. Berezovsky, R.M. Westervelt, Nanotechnology **21**, 274014 (2010)
31. S. Schnez, J. Guttinger, M. Huefner, C. Stampfer, K. Ensslin, T. Ihn, Phys. Rev. B **82**, 165445 (2010)
32. M.R. Connolly, K.L. Chiu, A. Lombardo, A. Fasoli, A.C. Ferrari, D. Anderson, G.A.C. Jones, C.G. Smith, Phys. Rev. B **83**, 115441 (2011)
33. N. Pascher, D. Bischoff, T. Ihn, K. Ensslin, Appl. Phys. Lett. **101**, 063101 (2012)
34. M.R. Connolly, R.K. Puddy, D. Logoteta, P. Marconcini, M. Roy, J.P. Griffiths, G.A.C. Jones, P.A. Maksym, M. Macucci, C.G. Smith, Nano Lett. **12**, 5448 (2012)
35. S. Bhandari, G.-H. Lee, A. Klales, K. Watanabe, T. Taniguchi, E. Heller, P. Kim, R.M. Westervelt, Nano Lett. **16**, 1690 (2016)
36. H. Sellier, B. Hackens, M.G. Pala, F. Martins, S. Baltazar, X. Wallart, L. Desplanque, V. Bayot, S. Huant, Semicond. Sci. Technol. **26**, 064008 (2011)
37. S. Washburn, H. Schmid, D. Kern, R.A. Webb, Phys. Rev. Lett. **59**, 1791 (1987)
38. R.A. Webb, S. Washburn, C.P. Umbach, R.B. Laibowitz, Phys. Rev. Lett. **54**, 2696 (1985)
39. F. Martins, B. Hackens, H. Sellier, P. Liu, M.G. Pala, S. Baltazar, L. Desplanque, X. Wallart, V. Bayot, S. Huant, Acta Phys. Polon. A **119**, 569 (2011)
40. B. Szafran, Phys. Rev. B **84**, 075336 (2011)

41. G.C. des Francs, C. Girard, J.C. Weeber, C. Chicane, T. David, A. Dereux, D. Peyrade, *Phys. Rev. Lett.* **86**, 4950 (2001)
42. C. Chicanne, T. David, R. Quidant, J.C. Weeber, Y. Lacroute, E. Bourillot, A. Dereux, G. Colas des Francs, C. Girard, Phys. Rev. Lett. **88**, 097402 (2002)
43. A. Cuche, O. Mollet, A. Drezet, S. Huant, Nano Lett. **10**, 4566 (2010)
44. E.J. Heller, Phys. Rev. Lett. **53**, 1515 (1984)
45. R.E. Prange, S.M. Girvin, *The Quantum Hall Effect*, 2nd edn. (Springer, New York, 1990)
46. V.J. Goldman, B. Su, Science **267**, 1010 (1995)
47. R.P. Taylor, A.S. Sachrajda, P. Zawadzki, P.T. Coleridge, J.A. Adams, Phys. Rev. Lett. **69**, 1989 (1992)
48. M. Kataoka, C.J.B. Ford, G. Faini, D. Mailly, M.Y. Simmons, D.R. Mace, C.-T. Liang, D.A. Ritchie, Phys. Rev. Lett. **83**, 160 (1999)
49. F.E. Camino, W. Zhou, V.J. Goldman, Phys. Rev. B **72**, 075342 (2005)
50. Y. Zhang, D.T. McClure, E.M. Levenson-Falk, C.M. Marcus, L.N. Pfeiffer, K.W. West, Phys. Rev. B **79**, 241304 (2009)
51. A.J.M. Giesbers, U. Zeitler, M.I. Katsnelson, D. Reuter, A.D. Wieck, G. Biasiol, L. Sorba, J.C. Maan, Nat. Phys. **6**, 173 (2010)
52. C. Zhou, M. Berciu, Phys. Rev. B **72**, 085306 (2005)
53. E. Peled, D. Shahar, Y. Chen, E. Diez, D.L. Sivco, A.Y. Cho, Phys. Rev. Lett. **93**, 236802 (2003)
54. N. Aoki, C.R. da Cunha, R. Akis, D.K. Ferry, Y. Ochiai, Phys. Rev. B **72**, 155327 (2005)
55. A. Baumgartner, T. Ihn, K. Ensslin, K.D. Maranowski, A.C. Gossard, Phys. Rev. B **76**, 085316 (2007)
56. A. Baumgartner, T. Ihn, K. Ensslin, G. Papp, F. Peeters, K.D. Maranowski, A.C. Gossard, Phys. Rev. B **74**, 165426 (2006)
57. N. Paradiso, S. Heun, S. Roddaro, D. Venturelli, F. Taddei, V. Giovannetti, R. Fazio, G. Biasiol, L. Sorba, F. Beltram, Phys. Rev. B **83**, 155305 (2011)
58. F. Martins, S. Faniel, B. Rosenow, M.G. Pala, H. Sellier, S. Huant, L. Desplanque, X. Wallart, V. Bayot, B. Hackens, New J. Phys. **15**, 013049 (2013)
59. F. Martins, S. Faniel, B. Rosenow, M.G. Pala, H. Sellier, S. Huant, L. Desplanque, X. Wallart, V. Bayot, B. Hackens, Sci. Rep. **3**, 1416 (2013)
60. H. Youn, M.T. Gastner, H. Jeong, Phys. Rev. Lett. **101**, 128701 (2008)
61. C.M. Penchina, L.J. Penchina, Am. J. Phys. **71**, 479 (2003)
62. D. Witthaut, M. Timme, New J. Phys. **14**, 083036 (2012)
63. M. Pala, H. Sellier, B. Hackens, F. Martins, V. Bayot, S. Huant, Nanoscale Res. Lett. **7**, 472 (2012)